applied sciences

IMPACT FACTOR 2.5

CITESCORE 5.5

Article

Validation of a Compact and Tunable Continuous Gas-Flow Laser-Plasma Target for Electron Beam Production Above 150 MeV

Pierre Drobniak, Jana Serhal, Maria Pia Anania, Elsa Baynard, Arnaud Beck, Christelle Bruni, Antoine Cauchois, Gemma Costa, Lucio Crincoli, Denis Douillet et al.

Special Issue

Trends and Prospects in Laser–Plasma Accelerator

Edited by

Dr. Mario Galletti and Dr. Livio Verra

MDPI

https://doi.org/10.3390/app16052312

applied sciences

MDPI

Article

Validation of a Compact and Tunable Continuous Gas-Flow Laser-Plasma Target for Electron Beam Production Above 150 MeV

Pierre Drobniak [1,*,†], Jana Serhal [1,*], Maria Pia Anania [2], Elsa Baynard [1], Arnaud Beck [3], Christelle Bruni [1], Antoine Cauchois [3], Gemma Costa [2], Lucio Crincoli [2], Denis Douillet [1], Julien Gautier [4], Jean-Philippe Goddet [4], Coline Guyot [1], Gregory Iaquaniello [1], Gueladio Kane [1], Sophie Kazamias [1], Olena Kononenko [4], Viacheslav Kubytskyi [1], Bruno Lucas [1], Ali Mahjoub [3], Antoine Maitrallain [5], Olivier Neveu [1], Yann Peinaud [1], Moana Pittman [1], Pascal Rousseau [4], Johan Sebastián Ramírez Amado [6], Arnd Specka [3], Cédric Thaury [4] and Kevin Cassou [1]

1 Laboratoire de Physique des 2 Infinis Irène Joliot-Curie (IJCLab), UMR 9012, CNRS, Université Paris-Saclay, 91400 Orsay, France
2 Laboratori Nazionali di Frascati, Via Enrico Fermi 54, 00044 Frascati, Italy
3 Laboratoire Leprince-Ringuet (LLR), UMR 7638, CNRS, Ecole Polytechnique, 91128 Palaiseau, France
4 Laboratoire d'Optique Appliquée (LOA), CNRS, École Polytechnique, ENSTA, Institut Polytechnique de Paris, 91120 Palaiseau, France
5 University of Bordeaux, CNRS, LP2I, UMR 5797, 33170 Gradignan, France
6 Graduate School de Physique, Université Paris-Saclay, Campus d'Orsay, Rue Louis de Broglie, 91400 Orsay, France
* Correspondence: pierre.drobniak@fys.uio.no (P.D.); jana.serhal@ijclab.in2p3.fr (J.S.)
† Current address: Department of Physics, University of Oslo, 0316 Oslo, Norway.

Abstract

The present article reports on the generation of stable 50 pC low-divergence electron beams above 150 MeV from laser-driven wakefield acceleration using a continuous-flow gas target prototype tested at the 60 TW Salle Jaune facility at LOA. The gas target design is meant to be easily transported and integrated as an element of the beamline with a differential pumping system offering some 10^{-4} mbar pressure in the rest of the line. A dedicated gas injection system allows for the control of the gas mixture concentration and gas pressure in two different regions of the target within the frame of controlled ionisation injection schemes. The measured electron beam parameters show the importance of gas density profiles and longitudinal gas mixture confinement.

Keywords: laser-plasma; electron source; gas target; injector; accelerator; experimental

Check for updates

Academic Editor: Atsushi Mase

Received: 31 December 2025
Revised: 14 February 2026
Accepted: 24 February 2026
Published: 27 February 2026

Copyright: © 2026 by the authors. Licensee MDPI, Basel, Switzerland. This article is an open access article distributed under the terms and conditions of the Creative Commons Attribution (CC BY) license.

1. Introduction

Theorised in the second half of the twentieth century [1–3], plasma acceleration nowadays aims to compete with radio-frequency (RF) technology. Due to its ionised state, plasma can achieve fields which exceed the usual 100 MV/m breakdown limit in RF and can sustain accelerating gradients that are many orders of magnitude higher. In 2007, Blumenfeld et al. [4] demonstrated at SLAC the energy doubling of an incoming 42 GeVelectron beam in 85 cm of plasma.

In addition to acceleration, plasma may also be used as an electron source or so-called "injector". In comparison with conventional photocathodes, laser-plasma injectors can produce electron bunches with much shorter bunch lengths (down to the sub-micron) [5–8]

and typical currents in the kA regime [9,10]. These features enable a wide range of applications, e.g., as an X-ray source for free-electron lasers (FELs) [11–13] or as a direct tool in medicine, such as Very High Energy Electrons (VHEE) therapy [14–17], potentially in combination with the FLASH effect [18], for localised selective dose deposition. Due to the strong focusing fields within the plasma-accelerating structure, electron beams from plasma injectors usually have a relatively small size (of the order of micrometers), which is counterbalanced by a large divergence at the exit. Combined with a broad energy spread, this makes them hard to transport. One solution is to have a smooth downramp of decreasing density, which slowly reduces the focusing field of the wake, as discussed in [19–24]. In the perfect-case scenario, the focusing force in the outramp remains linear and decreases slowly enough to act adiabatically on the beam, i.e., to preserve the transverse emittance. This slowly increases the beam size and decreases the divergence, making the free drift in vacuum after the source less critical for later capture.

As part of the European EuPRAXIA project [25], the PALLAS project at IJCLab [26] focuses on the design and testing of technological components for a laser-plasma injector, using the LASERIX facility [27] as the laser source. The objective is to demonstrate the operation of a stable and reliable electron beam with the following characteristics: 30 pC of charge, 150 MeV to 200 MeV of energy, a spread of less than 3%, emittance below 1 mm.mrad, and divergence below 1 mrad.

Since the PALLAS facility was not yet operational at the time of the experiment, the target design was tested at the Salle Jaune laser facility at LOA. It delivers high-stability laser pulses at 800 nm, with a typical pulse duration of 30 fs and peak powers reaching up to 60 TW after compression. The Salle Jaune facility is a highly versatile platform dedicated to laser-plasma acceleration and ultrafast radiation science. It supports the production of electron beams spanning a wide range of parameters, from multi-nanocoulomb bunches at a few MeV [28] to a few pC at energies exceeding 1 GeV [29]. The facility is also used to generate ultrabright X-ray sources through Compton scattering [30,31] and betatron radiation [32,33]. These sources enable a wide range of applications, including the investigation of warm dense matter [34,35] and studies in radiobiology [36,37].

We propose here a design that operates in continuous gas flow and which is meant to be easily transportable, as a part of the beamline. Such an approach brings novelty to the community, approaching an easy integration of laser-plasma electron sources.

We begin by introducing the laser-plasma electron source design in Section 2, along with the setup used to test it. The experimental results of electron beam production are presented in Section 3, with an emphasis on stability and divergence (Section 3.1). We then improve their spectra through gas mixture and pressure control in Section 3.2. Finally, we conclude on the results presented and propose future developments for the target design.

2. Materials and Methods

2.1. Target Design

To fulfil the laser-plasma electron source parameters, we choose the self-truncated ionisation injection technique [38,39]. The target has a first region where a dopant (high-Z gas, like N_2) is mixed with a background gas (typically He). A laser pulse ionises the region and creates a plasma wake. When the laser becomes intense enough, the inner-shell electrons of the high-Z gas may be trapped inside the wake and accelerated. The target's second region only contains a background gas, preventing dopant injection and serving as an accelerating stage for the injector.

The gas cell we use as a laser-plasma electron source is presented in Figure 1. It is inspired by the design used by the LUX team at DESY [10] mixed with the design from Kim et al. [40].

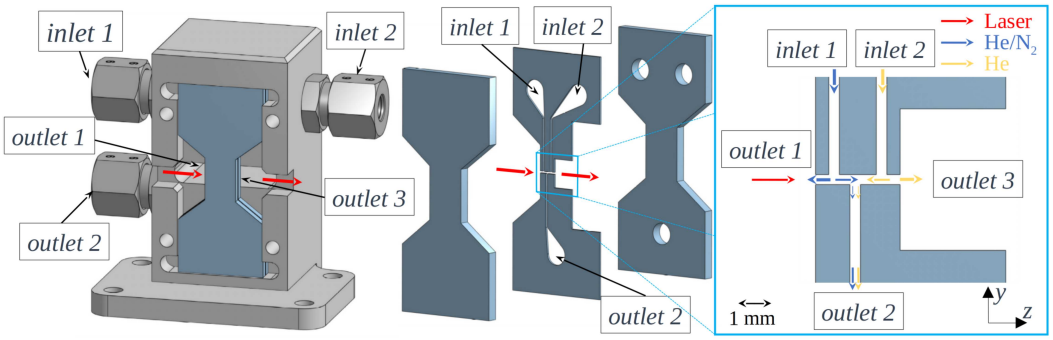

Figure 1. 3D schematic of the cell with its holder (light grey). Helium mixed with nitrogen and pure helium are injected, respectively, through *inlet 1* and *inlet 2*. *Outlet 1* and *outlet 3* are regions of longitudinal exhaust for the gas, and *outlet 2* serves as a transverse pumping channel to control the mixing of the injected gases.

It consists of three plates glued together. The two quartz outer plates have optical quality to allow for diagnostics. The central one is made of ceramic (Al_2O_3) and has inner features that, once mounted with the two outer plates, correspond to channels for a gas inlet, an outlet, and a central longitudinal plasma channel with a 500×500 µm cross-section. Transverse optical diagnostics can be performed for the plasma density profile at low laser energy.

Our objective is to have two distinct regions: the first (*region 1*) fed through *inlet 1* (at $z = -0.800$ mm) with He doped with N_2 for electron injection and the second (*region 2*) fed through *inlet 2* (at $z = +1.00$ mm) with pure He for electron acceleration. The gas flows and dopant concentration can be varied with a 0.5 s response time through a dedicated gas injection system monitored and controlled by pressure gauges and mass flow controllers, allowing continuous concentration tuning from 1.5% to 100% and pressure ranging from 10 ± 0.12 mbar to 150 ± 0.45 mbar (RMS evaluated over a 3 min continuous operation), evaluated on an axis using fluid simulation. A central outlet *outlet 2* ($z = 0$ mm) between the two regions allows for better control of the mixing interface.

Relativistic self-focusing in a plasma (decrease in laser waist, increase in intensity) is triggered when the laser power exceeds the critical power $P_c[\mathrm{GW}] \approx 17.4(\lambda_p/\lambda_L)^2$ [41], with λ_p and λ_L denoting the plasma and laser wavelength, respectively. For a typical 50 TW pulse, this happens for a fully ionised He pressure above 12 mbar. In order to avoid early self-focusing, which could lead to a long and uncontrolled electron injection, we decided to have a sharp opening at the cell entrance to keep the gas upramp as short as possible. On the contrary, the exit has a long, low-gas-density tail which slowly decreases the focusing strength on the beam and controls its divergence.

The target lifetime depends on hazardous alignment errors. The current data were collected using a single target with over 3800 laser shots, and the target remained functional.

2.2. Integration in the Beamline

The cell holder from Figure 1 is inserted inside a 14×14 cm vacuum cube, as presented in Figure 2, with two apertures (3 mm diameter) that allow the laser to pass through and provide differential pumping between the cube and the rest of the beamline.

A vacuum pumping system connected to the cube enables continuous-gas-injection-mode operation at around 100 mbar. The pressure in the differential pumping cube rises up to 1.2 mbar, and the rest of the beam line remains at a relatively low level, rising from 3×10^{-5} mbar (no gas injection) to 3×10^{-4} mbar (gas injection) with the standard secondary pumps. Optical quality windows allow for in-air optical transverse diagnostics.

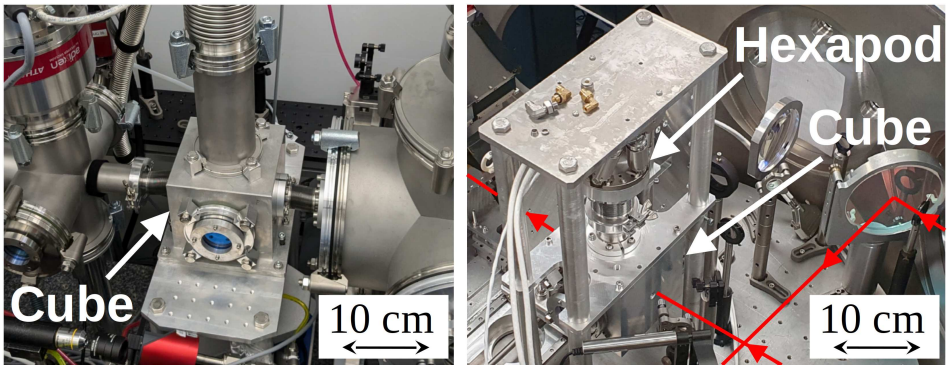

Figure 2. Integration in the beamline of the cube for: its usual use with bellows within the PALLAS project (**left**) and its upside-down in-vacuum modified version for the LOA campaign (**right**). A hexapod allows for the independent motion of the cell inside the cube in all directions. The laser path for the LOA set-up is depicted in red.

This cube can be easily transported and integrated as a direct element of the beamline with bellows connections, as for the PALLAS project (Figure 2, left). For the specific experiment at LOA, the design had to be inserted inside a large vacuum chamber (1.5 m diameter, 1 m height). It was then modified, with a main structure that maintains the cube upside down and a hexapod with a vacuum motion feedthrough, allowing the independent motion of the cell holder (Figure 2, right).

2.3. Set-Up Used at LOA

A schematic of the set-up used at LOA is presented in Figure 3.

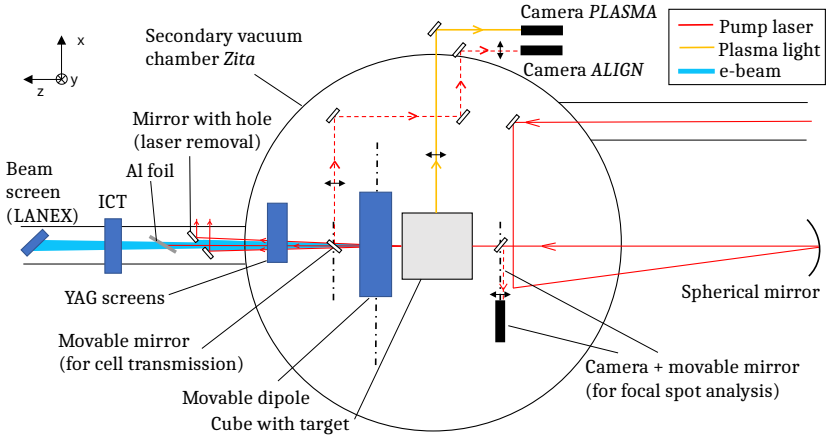

Figure 3. Schematic of the experimental setup of the gas cell target interaction chamber and electron beam diagnostics used at LOA.

The P-polarised (along x) laser was tuned to deliver pulses with a duration of $T_{FWHM}^{(exp)} = 32 \pm 2$ fs at wavelength $\lambda_L = 810$ nm, with 1.5 ± 0.2 J energy (50 TW) at 1 Hz, focused with a 1.5 m focal length spherical mirror. The pulse is estimated to be a 5th-order Flattened Gaussian Beam (FGB) [42], with a waist in vacuum of $w_{0,vac}^{(exp)} = 17 \pm 2$ µm inside the cell, which corresponds to a Rayleigh length $\lambda_R^{(exp)} \approx 1$ mm.

We estimate the normalised vector potential, a_0, in vacuum to be around $a_{0,vac}^{(exp)} = 1.7$. Such a value is not enough to reach the barrier suppression ionisation (BSI) threshold of N^{5+} and N^{6+}, respectively, of 2.21 and 2.77 at 800 nm [43]. However, if the plasma wavelength λ_p is short enough (i.e., if the density is high enough), the laser power can exceed the so-called "critical power" for self-focusing (given in Section 2.1), which is the case for our injector once the pulse starts entering *region 1*.

An ISP deformable mirror composed of 33 piezo motors for wavefront correction is located 10.6 m upstream of the spherical mirror and allows the focal plane to be shifted along the optical axis within a $[-2.5, +4.5]$ mm range, with 0 corresponding to the centre of *outlet 2*. The laser-pointing stability is evaluated to be ± 15 µrad. This corresponds to a variation of roughly a spot size in all transverse directions at the cell entrance. The laser is removed after the electron spectrometer, approximately 75 cm from the cell exit, using a mirror with a hole (10 mm in diameter), followed by a 25 µm-thick grazing incidence aluminium foil.

As presented in Figure 3, several cameras are used for laser and plasma diagnostics: a camera with a movable mirror for focal spot analysis at the cube entrance, a camera (*ALIGN*) with a movable mirror for the alignment of the cell, and a camera (*PLASMA*) for the live visualisation of the target.

The electron beams are monitored in:

- Energy with an electron spectrometer consisting of a 1.5 T, a 10 cm movable dipole magnet with two YAG:Ce screens, imaged on an Allied vision PROSILICA GT 1290 camera (Allied Visions GmH, Stadtroda,Germany), positioned, respectively, at 14 cm, 30 cm and 40 cm downstream of the target, enabling electron energy measurements above 140 MeV with an error increasing from 5 to 80 MeV (per mm of entrance jitter in dispersive direction) at energies from 140 to 500 MeV;
- A charge with an integrating current transformer (ICT) for charge measurement above 60 MeV (we estimate from PIC simulations the energies below 60 MeV to be too divergent to pass through the mirror with a hole) with a [0.5–300] pC range and a typical signal-to-noise ratio (SNR) above 50, placed at 148 ± 5 cm from the source;
- Divergence and pointing stability with a beam screen, composed of a LANEX scintillator screen (Kodak GmbH, Stuttgart, Germany) mounted on a thin aluminium frame, imaged onto a Basler acA640-120gm CCD camera (Basler AG, Ahrensburg, Germany), positioned at 167 ± 1 cm from the source at the end of the beamline.

Those diagnostics cannot be used simultaneously and, therefore, require repeating the shot series. For some series, however, data were recorded only on the spectrometer screen. In that case, the screen intensity, cross-calibrated with ICT measurements, can be used to estimate the charge. The spectrometer-screen data also provide the divergence component transverse to the beam-dispersion direction of the dipole.

3. Results

3.1. Stable and Low-Divergence Beams

We present a series of 10 consecutive shots in Figure 4, obtained with a dopant concentration of $c_{N_2} = 14.6\%$ and pressures of $P_1 = 125$ mbar and $P_2 = 121$ mbar, corresponding to a pressure gradient on axis $\Delta P = -4$ mbar. The laser is focused around the centre of *inlet 2*. Since the Rayleigh length is approximately 1 mm, the laser intensity is high enough to trigger self-focusing in the density upramp so that a_0 in the plasma actually becomes high enough to ionise N^{5+} and N^{6+} and inject their electrons in the plasma wake.

This series shows a typical spectrum stability with 10% fluctuation. The estimated charge is 50 ± 25 pC (RMS). All spectra displayed in Figure 4, however, exhibit both a high and a low energy feature, characterised by two distinct energy populations: one long tail centred at approximately 200 MeV and a peak at approximately 360 MeV.

We performed PIC simulations to find the origin of those two energy populations. The code used is SMILEI [44], with an envelope approximation and cylindrical symmetry with one azimuthal mode. Species are initialised as ionised up to He^{2+} and N^{5+}, ionisation is modelled from the envelope model coupled with tunnel ionisation rates [45], and we use 1 particle per cell to track the species (such an approximation was already discussed

in [46]). The laser is modelled as a 5th-order FGB, with a duration of $T_{FWHM}^{(sim)} = 35$ fs, a waist in vacuum of $w_{0,vac}^{(sim)} = 15$ µm, and energy of 1.5 J, resulting in an a_0 in vacuum of $a_{0,vac}^{(sim)} = 1.7$.

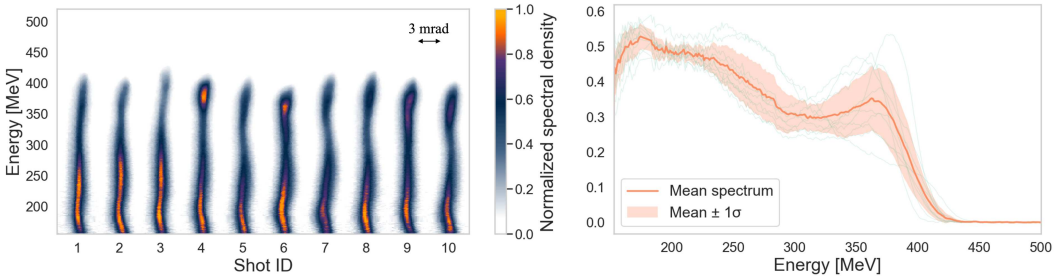

Figure 4. 2D waterfall of 10 experimental spectra (**left**), together with their 1D overlapping plots (**right**), obtained with settings: $P_1 = 125$ mbar, $P_2 = 121$ mbar ($\Delta P = -4$ mbar), $c_{N_2} = 14.6\%$ and a laser focused in vacuum at the centre of *outlet 2*. Two narrow peaks at fixed energies (∼170 MeV and ∼230 MeV), consistently present across all shots and attributed to light scattering, were corrected through interpolation between nearby uncontaminated energy bins. The 1D plots correspond to the charge density integrated over a 3 mrad window, centred on the density peak for each energy slice.

The density profiles and mixing are assessed with OpenFOAM [47] simulations. Since we did not find a solver that combines both compressibility and diffusion, we proceeded in two steps, with two different solvers, as already proposed in [48]. First, *rhoPimpleFoam* [49] (compressible, non-miscible) assesses the main density profile, accounting for the compressibility effect, which is especially necessary in the up-/down-ramps. Its output is then used as input for *interMixingFoam* [50] (incompressible, miscible), which models dopant mixing at the interface between *regions 1* and *2*. Our simulation data are left open and available on a Git repository [51].

We set the simulation settings to: $P_1 = 125.57$ mbar, $P_2 = 121.57$ mbar, $x_{\text{off}} = +1294$ µm ($x_{\text{off}} = 0$ corresponds to the centre of *outlet 2*), and $c_{\text{N}_2} = 14\%$, which are similar to the experimental ones in Figure 4. In order to investigate the importance of the dopant mixing interface, we also simulated the case with $\Delta P = 0$ for comparison. The simulation results are displayed in Figure 5.

Simulations reveal that the laser undergoes strong self-focusing, which is not optimal for a controlled injection. Its normalised intensity goes from below 2 in vacuum to approximately 4 in *region 1* and then 6 inside *region 2*. This originates from a high density in the cell.

In both cases, the bunch is accelerated to approximately $z = 1$ mm. The energy then decreases, first due to dephasing within the laser-driven bubble, and then transitions to a beam-driven decelerating regime (the laser is not intense enough to drive a wakefield). From $z = 0$, the energy spread already begins to increase due to the non-optimally loaded bubble, yielding a gradient in the accelerating field, E_z, as is visible at $z = 0.27$ mm. For the $\Delta P = -4$ mbar case, the energy spread increase is even more pronounced. This originates from a higher plasma density inside *region 2* from dopant leakage (N_2 not confined inside *region 1*), shortening the bubble and creating a steeper gradient in E_z. The origin of the splitting into two energy populations for the $\Delta P = -4$ mbar case very likely comes from an original spatial splitting which then translates into two distinct energy populations when accelerated with a gradient in E_z, as is visible in the positively chirped longitudinal phase space at $z = 4$ mm (Figure 5c).

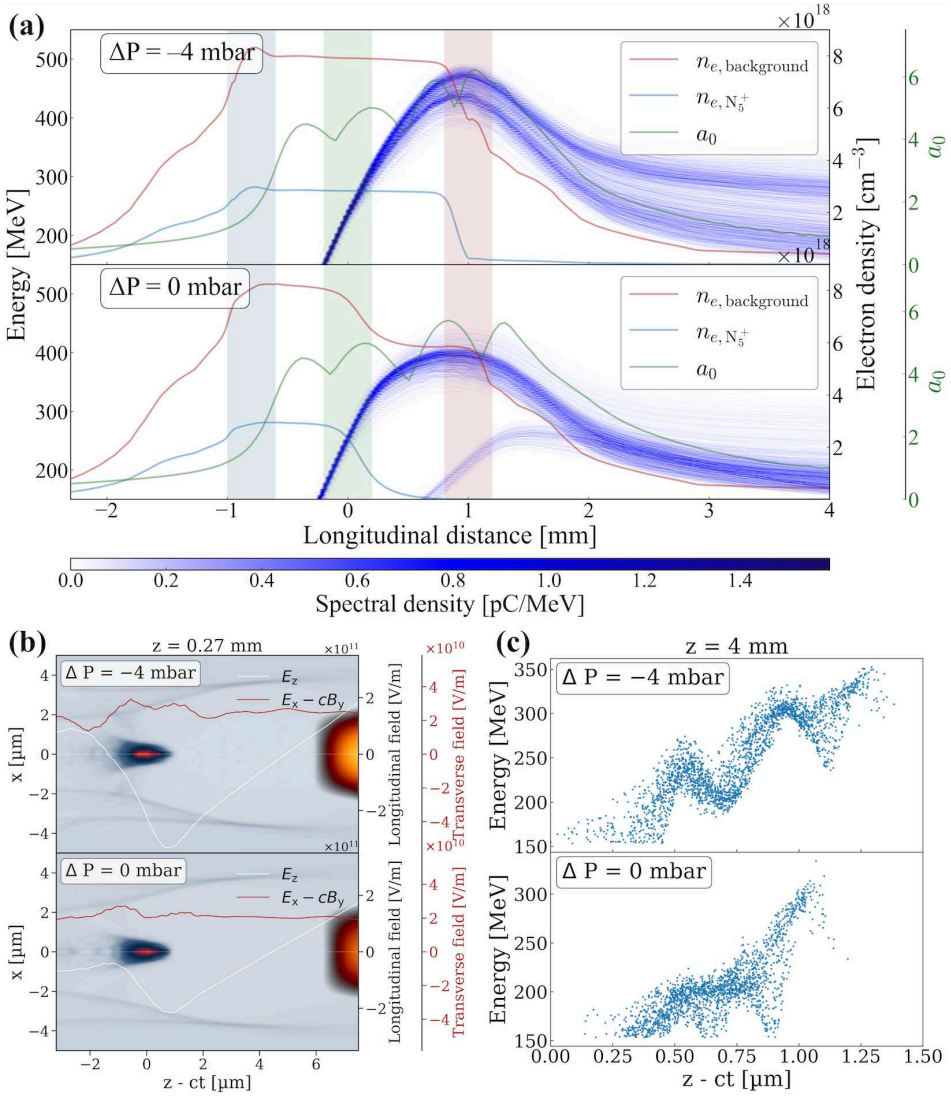

Figure 5. PIC simulations comparing cases with $\Delta P = -4$ mbar and $\Delta P = 0$ mbar. The energy spectrum for electrons with a final energy of $E > 150$ MeV, together with the laser a_0 in plasma and the electron density profiles $n_{e,background}$ (fully ionised He and five first levels of N) and $n_{e,N^{5+}}$ (five first levels of N only) are displayed (**a**), with blue, green and red shaded regions corresponding to *inlet 1*, *outlet 2*, and *inlet 2*, respectively. The final total charge above 150 MeV is 26.96 pC ($\Delta P = -4$ mbar) and 21.08 pC ($\Delta P = 0$ mbar). The beam and bubble are extracted inside *region 2*, and the accelerating and focusing fields are added (**b**). The longitudinal phase space at $z = 4$ mm is shown (**c**). For both cases, the dopant concentration is $c_{N_2} = 14\%$, and the laser focused at $x_{\text{off}} = 1294$ µm (0 corresponds to the centre of *outlet 2*). The pressures used are: $P_1 = 125.57$ mbar and $P_2 = 121.57$ mbar ($\Delta P = -4$ mbar case), and $P_1 = P_2 = 121.12$ mbar ($\Delta P = 0$ mbar case).

The experimental beam pointing stability measured on the beam screen from a consecutive series of 18 shots with the same target parameters is evaluated to be $(0.78, 0.60)$ mrad RMS in (x, y), which is the state of the art [10,52–55]. Electron beam pointing variation may originate from the laser wavefront and pulse front tilt stability, which may change the laser propagation together with the injection condition and bubble shape from shot to shot [56,57]. The slight asymmetry can be explained by the laser polarisation along x.

The experimental RMS divergence evaluated over 18 consecutive shots from the same conditions is $(\sigma_{x'}, \sigma_{y'}) = (1.23 \pm 0.21, 0.60 \pm 0.09)$ mrad in (x, y) (higher value in the laser polarisation direction, explained by an additional initial transverse momentum imparted to the electrons at the moment of their ionisation from the laser field, as already observed

in [10,54,58]). This competes with other experimental results using a similar injector and presenting a typical divergence in the [0.5–1.0] mrad range [10].

The evolution of the divergence in the outramp is extracted from the PIC simulation for $\Delta P = -4$ mbar and presented in Figure 6.

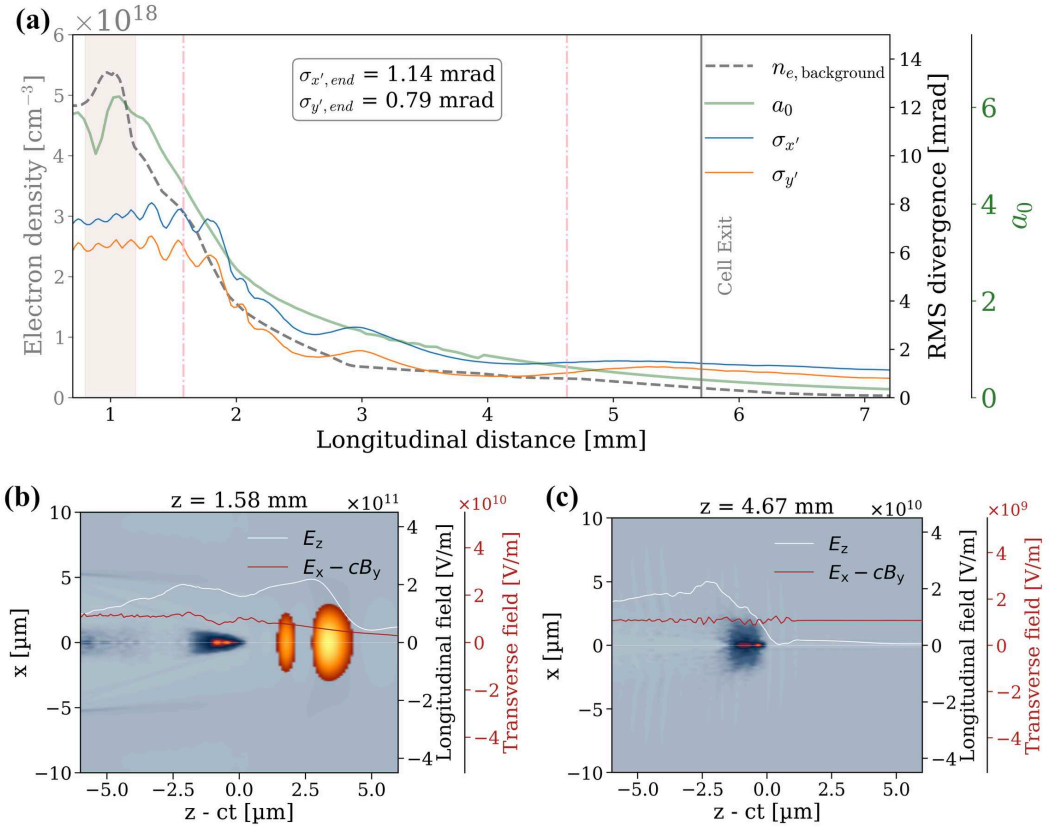

Figure 6. PIC simulation using parameters from the Figure 5 case at $\Delta P = -4$ mbar, zoomed in at the plasma outramp. Sub-graph (**a**) displays the evolution of plasma density (grey dotted line), laser normalised intensity in plasma $a_{0,plasma}^{(sim)}$ (green line), and RMS beam divergence $\sigma_{x'}$ (blue line) and $\sigma_{y'}$ (orange line). The location of *inlet* 2 is indicated by a red shaded region. The bottom sub-graphs are 2D screenshots extracted at $z = 1.58$ mm (**b**) and $z = 4.63$ mm (**c**), which display the laser pulse, the accelerated bunch, the plasma density, the transverse field $E_x - cB_y$, and the accelerating field E_z.

While the bubble was laser-driven and accelerating in *region* 2, it transitions after $z = 1$ mm into a transitional regime where both the dephased laser and the accelerated beam contribute to the wakefield formation (Figure 6b). The regime then fully becomes beam-driven after $z = 3$ mm (Figure 6c). In both cases, the wakefield is decelerating and focusing. The divergence is progressively reduced below 1 mrad, with a slightly higher value in the laser polarisation direction x. The particular case of beam-driven divergence control is explained by a passive plasma lensing effect, as already presented in [19–24].

The emittance is evaluated using PIC simulation (no quadrupole scans possible or additional screens available in the experiment), and filters out particles below 150 MeV. The values are $(\epsilon_x, \epsilon_y) = (2.86, 1.77)$ mm.mrad and $(\epsilon_x, \epsilon_y) = (1.29, 0.62)$ mm.mrad, for $z = 1.58$ mm and $z = 4.63$ mm, respectively. For the same reasons as for the divergence, the emittance is higher in x than y.

3.2. Spectrum Improvement Through Dopant Control

Although the beams presented in Section 3.1 have interesting features, such as low RMS values for pointing stability and divergence, their spectra, shown in Figure 4, have a large low-energy tail, which is not desirable for beam transport since chromatic effects

will eventually result in charge loss [19]. We, therefore, experimentally scan the helium gas pressure P_2 between 80 and 105 mbar while keeping P_1 constant at around 100 mbar, with a slightly reduced dopant concentration, $c_{N_2} = 6.67\%$, in order to see the effect of ΔP on dopant confinement and subsequently on the electron density inside *region 2*. The resulting spectra are presented in Figure 7.

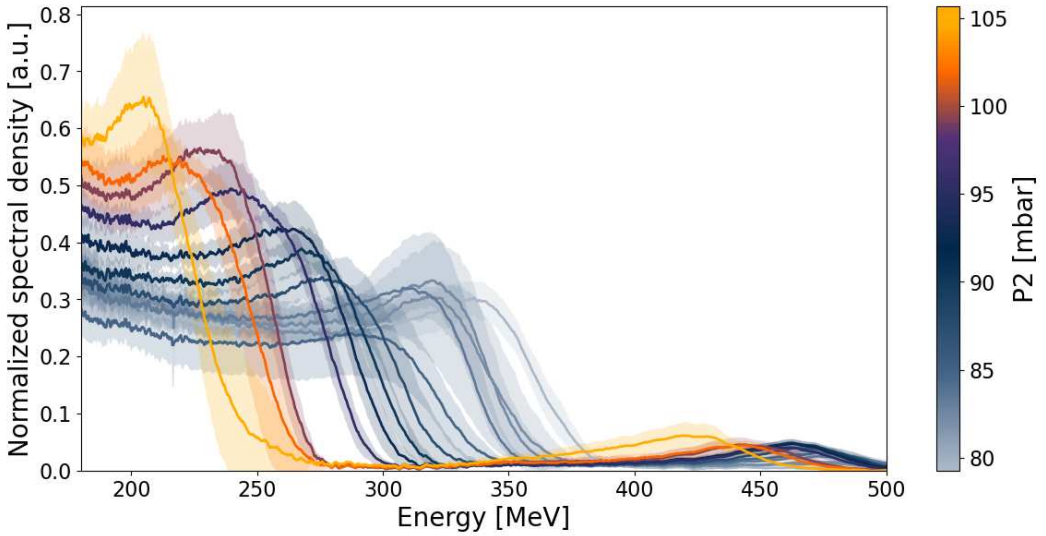

Figure 7. Experimental spectra obtained at different pressures, P_2, while maintaining a constant pressure, $P_1 = 105$ mbar. The dopant concentration is kept constant at $c_{N_2} = 6.67\%$, and the laser is focused at the centre of *inlet 2*. Each curve represents the mean of the 1D spectra over 10 consecutive shots with clouds displaying the 1-sigma variation. For a shot, the 1D spectrum is obtained from the integration of charge density across a 3 mrad window, centred around the density peak for each energy slice. All shots led to injection, i.e., a 100% success rate.

All spectra displayed in Figure 7 have a plateau shape ending with a local maximum, followed by a sharp cut-off. We attribute this broad shape to a non-optimally loaded bubble. In addition, a high-energy population appears between 430 and 470 MeV. This series of spectra, however, shows a regular and remarkable behaviour with P_2.

When increasing P_2, the energy shifts towards lower values, from a local maximum of around 350 MeV down to 220 MeV, but with a higher spectral density. The high-energy population also shifts towards slightly lower energies and increases in spectral density, similarly to the local maximum. We attribute this effect to the increasing dopant confinement inside *region 1* with an increasing P_2. This corresponds to a lower electron density inside *region 2* and, thus, a reduced accelerating field.

The charge is about 50 pC for all cases, which is comparable to the results from Figure 5. The RMS divergence evaluated on the spectrometer screen evolves from 1.57 ± 0.1 mrad ($\Delta P = -25$ mbar) to 2.05 ± 0.15 mrad (for $\Delta P = 0$ mbar), which is greater than in Section 3.1. The reduction in the dopant concentration, together with its progressive confinement inside *region 1*, decreases the length of the downramp, thus acting more shortly on the divergence and resulting in larger values than for Figure 5.

4. Conclusions

A continuous-flow gas target was designed and tested for ionisation injection in a laser-driven wakefield. The design allows for easy transport and integration as a direct element of the beamline or in a large interaction vacuum chamber. Fluid simulations have highlighted the capabilities of our design to control both the pressure over a large range and the dopant location inside the target.

The initial results demonstrate electron beams with sub-mrad pointing and divergence above 150 MeV, reflecting the stable gas species distribution in the target. However, under non-fully optimised injection conditions, the beams exhibit two distinct energy populations. The mechanism behind this splitting is explained using PIC simulations. Their low final divergence is achieved through a long, low-density tail, which eventually acts as a passive plasma lens.

Using a dedicated gas injection system, the pressure differences between the gas mixture and the background gas (He), as well as the dopant (N_2) concentration in the mixture, were varied. Increasing the pressure difference up to $\Delta P = 0$ mbar results in a dopant confined inside *region 1*, which lowers the density inside *region 2*, yielding well-defined and more peaked spectra. The gas target operates in a high-vacuum environment across a wide pressure range in continuous flow, making it a viable integration option for high-repetition-rate laser wakefield accelerator setups.

Investigating lower pressures would have allowed for a reduction in the observed strong self-focusing, resulting in a more localised injection, as proposed from PIC simulations in [46], and very likely well-defined lower energy spread bunches. A deeper investigation into the laser control could even improve the longitudinal focal spot positioning and the relatively good pointing stability. The divergence can be reduced by testing other output geometries. Further experiments on the now-operational PALLAS test facility will allow for more dedicated beam time, providing an opportunity to obtain additional data for optimisation.

Author Contributions: Conceptualisation: M.P.A., A.B., C.B., K.C., A.C., G.C., L.C., D.D., P.D., J.G., J.-P.G., C.G., G.I., G.K., S.K., O.K., V.K., B.L., A.M. (Ali Mahjoub), A.M. (Antoine Maitrallain), O.N., Y.P., M.P., P.R., A.S. and C.T.; methodology: K.C., P.D., G.K. and J.S.; software: K.C., P.D., C.G., G.K., O.N., P.R. and J.S.; validation: K.C., P.D., G.K., S.K. and J.S.; formal analysis: K.C., P.D. and J.S.; investigation: E.B., K.C., A.C., G.C., L.C., D.D., P.D., J.G., J.-P.G., C.G., G.I., G.K., S.K., O.K., V.K., B.L., A.M. (Ali Mahjoub), A.M. (Antoine Maitrallain), O.N., Y.P., M.P., P.R., J.S.R.A., J.S., A.S. and C.T.; resources: E.B., M.P.A., A.C., A.B., C.B., P.D., D.D., J.G., J.-P.G., G.I., G.K., S.K., O.K., V.K., B.L., A.M. (Ali Mahjoub), A.M. (Antoine Maitrallain), Y.P., M.P., J.S.R.A., P.R., A.S., C.T. and K.C.; data curation: K.C., G.K.,O.N. and J.S.; writing—original draft preparation: K.C., P.D., S.K. and J.S.; writing—review and editing: K.C., P.D., J.S. and S.K.; visualisation: P.D. and J.S.; supervision: K.C., S.K. and C.T.; project administration: K.C. and C.T.; funding acquisition: K.C. and C.T. All authors have read and agreed to the published version of the manuscript.

Funding: This research was funded by State funding managed by the Agence National de la Recherche (ANR) under the Programme d'Investissements d'Avenir (Future Investment Programme) with the reference PACIFICS ANR-21-ESRE-0049 program and by EUPRAXIA-PP HORIZON-INFRA-2021-DEV-02 EUR project 101079773. This work was granted access to the HPC resources of TGCC under the allocations 2021-A0110510062 and 2022-A0130510062 made by GENCI for the project Virtual Laplace.

Institutional Review Board Statement: Not applicable.

Informed Consent Statement: Not applicable.

Data Availability Statement: The data presented in this study are openly available in CFD simulations for LPA target (https://gitlab.in2p3.fr/cfd-simulations-lpa-target (accessed on 23 February 2026)).

Acknowledgments: We acknowledge LOA teams for the laser beamtime and support for the experimental campaign. This work was granted access to the HPC resources of TGCC under the allocations 2021-A0110510062 and 2022-A0130510062 made by GENCI for the project Virtual Laplace.

Conflicts of Interest: The authors declare no conflicts of interest.

References

1. Fainberg, I.B. The use of plasma waveguides as accelerating structures in linear accelerators. In Proceedings of the CERN Symposium on High-Energy Accelerators and Pion Physics (1st International Conference on High-Energy Accelerators, HEACC 1956), Geneva, Switzerland, 11–23 June 1956.
2. Tajima, T.; Dawson, J.M. Laser electron accelerator. *Phys. Rev. Lett.* **1979**, *43*, 267. [CrossRef]
3. Chen, P.; Dawson, J.M.; Huff, R.W.; Katsouleas, T. Acceleration of electrons by the interaction of a bunched electron beam with a plasma. *Phys. Rev. Lett.* **1985**, *54*, 693. [CrossRef] [PubMed]
4. Blumenfeld, I.; Clayton, C.E.; Decker, F.J.; Hogan, M.J.; Huang, C.; Ischebeck, R.; Iverson, R.; Joshi, C.; Katsouleas, T.; Kirby, N.; et al. Energy doubling of 42 GeV electrons in a metre-scale plasma wakefield accelerator. *Nature* **2007**, *445*, 741–744. [CrossRef]
5. van Tilborg, J.; Schroeder, C.B.; Filip, C.V.; Tóth, C.; Geddes, C.G.R.; Fubiani, G.; Huber, R.; Kaindl, R.A.; Esarey, E.; Leemans, W.P. Temporal Characterization of Femtosecond Laser-Plasma-Accelerated Electron Bunches Using Terahertz Radiation. *Phys. Rev. Lett.* **2006**, *96*, 014801. [CrossRef]
6. Debus, A.D.; Bussmann, M.; Schramm, U.; Sauerbrey, R.; Murphy, C.D.; Major, Z.; Hörlein, R.; Veisz, L.; Schmid, K.; Schreiber, J.; et al. Electron Bunch Length Measurements from Laser-Accelerated Electrons Using Single-Shot THz Time-Domain Interferometry. *Phys. Rev. Lett.* **2010**, *104*, 084802. [CrossRef]
7. Buck, A.; Nicolai, M.; Schmid, K.; Sears, C.M.; Sävert, A.; Mikhailova, J.M.; Krausz, F.; Kaluza, M.C.; Veisz, L. Real-time observation of laser-driven electron acceleration. *Nat. Phys.* **2011**, *7*, 543–548. [CrossRef]
8. Huang, K.; Jin, Z.; Nakanii, N.; Hosokai, T.; Kando, M. Electro-Optic 3D Snapshot of a Laser Wakefield Accelerated Kilo-Ampere Electron Bunch. *Light Sci. Appl.* **2024**, *13*, 84. [CrossRef]
9. Couperus, J.; Pausch, R.; Köhler, A.; Zarini, O.; Krämer, J.; Garten, M.; Huebl, A.; Gebhardt, R.; Helbig, U.; Bock, S.; et al. Demonstration of a beam loaded nanocoulomb-class laser wakefield accelerator. *Nat. Commun.* **2017**, *8*, 487. [CrossRef]
10. Kirchen, M.; Jalas, S.; Messner, P.; Winkler, P.; Eichner, T.; Hübner, L.; Hülsenbusch, T.; Jeppe, L.; Parikh, T.; Schnepp, M.; et al. Optimal beam loading in a laser-plasma accelerator. *Phys. Rev. Lett.* **2021**, *126*, 174801. [CrossRef]
11. Wang, W.; Feng, K.; Ke, L.; Yu, C.; Xu, Y.; Qi, R.; Chen, Y.; Qin, Z.; Zhang, Z.; Fang, M.; et al. Free-electron lasing at 27 nanometres based on a laser wakefield accelerator. *Nature* **2021**, *595*, 516–520. [CrossRef] [PubMed]
12. Labat, M.; Cabadağ, J.C.; Ghaith, A.; Irman, A.; Berlioux, A.; Berteaud, P.; Blache, F.; Bock, S.; Bouvet, F.; Briquez, F.; et al. Seeded free-electron laser driven by a compact laser plasma accelerator. *Nat. Photonics* **2023**, *17*, 150–156. [CrossRef]
13. Galletti, M.; Assmann, R.; Couprie, M.; Ferrario, M.; Giannessi, L.; Irman, A.; Pompili, R.; Wang, W. Prospects for free-electron lasers powered by plasma-wakefield-accelerated beams. *Nat. Photonics* **2024**, *18*, 780–791. [CrossRef]
14. DesRosiers, C.; Moskvin, V.; Bielajew, A.F.; Papiez, L. 150–250 MeV electron beams in radiation therapy. *Phys. Med. Biol.* **2000**, *45*, 1781. [CrossRef]
15. Glinec, Y.; Faure, J.; Malka, V.; Fuchs, T.; Szymanowski, H.; Oelfke, U. Radiotherapy with laser-plasma accelerators: Monte Carlo simulation of dose deposited by an experimental quasimonoenergetic electron beam. *Med Phys.* **2006**, *33*, 155–162. [CrossRef] [PubMed]
16. Guo, Z.; Liu, S.; Zhou, B.; Liu, J.; Wang, H.; Pi, Y.; Wang, X.; Mo, Y.; Guo, B.; Hua, J.; et al. Preclinical tumor control with a laser-accelerated high-energy electron radiotherapy prototype. *Nat. Commun.* **2025**, *16*, 1895. [CrossRef] [PubMed]
17. Labate, L.; Palla, D.; Panetta, D.; Avella, F.; Baffigi, F.; Brandi, F.; Di Martino, F.; Fulgentini, L.; Giulietti, A.; Köster, P.; et al. Toward an effective use of laser-driven very high energy electrons for radiotherapy: Feasibility assessment of multi-field and intensity modulation irradiation schemes. *Sci. Rep.* **2020**, *10*, 17307. [CrossRef] [PubMed]
18. Favaudon, V.; Caplier, L.; Monceau, V.; Pouzoulet, F.; Sayarath, M.; Fouillade, C.; Poupon, M.F.; Brito, I.; Hupé, P.; Bourhis, J.; et al. Ultrahigh dose-rate FLASH irradiation increases the differential response between normal and tumor tissue in mice. *Sci. Transl. Med.* **2014**, *6*, 245ra93. [CrossRef] [PubMed]
19. Migliorati, M.; Bacci, A.; Benedetti, C.; Chiadroni, E.; Ferrario, M.; Mostacci, A.; Palumbo, L.; Rossi, A.; Serafini, L.; Antici, P. Intrinsic normalized emittance growth in laser-driven electron accelerators. *Phys. Rev. Spec. Top. Beams* **2013**, *16*, 011302. [CrossRef]
20. Sears, C.M.; Buck, A.; Schmid, K.; Mikhailova, J.; Krausz, F.; Veisz, L. Emittance and divergence of laser wakefield accelerated electrons. *Phys. Rev. Spec. Top. Beams* **2010**, *13*, 092803. [CrossRef]
21. Kuschel, S.; Hollatz, D.; Heinemann, T.; Karger, O.; Schwab, M.; Ullmann, D.; Knetsch, A.; Seidel, A.; Rödel, C.; Yeung, M.; et al. Demonstration of passive plasma lensing of a laser wakefield accelerated electron bunch. *Phys. Rev. Accel. Beams* **2016**, *19*, 071301. [CrossRef]
22. Doss, C.E.; Adli, E.; Ariniello, R.; Cary, J.; Corde, S.; Hidding, B.; Hogan, M.J.; Hunt-Stone, K.; Joshi, C.; Marsh, K.A.; et al. Laser-ionized, beam-driven, underdense, passive thin plasma lens. *Phys. Rev. Accel. Beams* **2019**, *22*, 111001. [CrossRef]
23. Chang, Y.Y.; Cabadağ, J.C.; Debus, A.; Ghaith, A.; LaBerge, M.; Pausch, R.; Schöbel, S.; Ufer, P.; Schramm, U.; Irman, A. Reduction of the electron-beam divergence of laser wakefield accelerators by integrated plasma lenses. *Phys. Rev. Appl.* **2023**, *20*, L061001. [CrossRef]

24. Steyn, T.; Panchal, A.; Vasilovici, O.; Schöbel, S.; Ufer, P.; Herrmann, F.; Chang, Y.Y.; Moulanier, I.; Masckala, M.; Khomyshyn, O.; et al. Observation of laser plasma accelerated electrons with transverse momentum spread below the thermal level. *arXiv* **2025**, arXiv:2506.18047. [CrossRef]
25. Assmann, R.; Weikum, M.; Akhter, T.; Alesini, D.; Alexandrova, A.; Anania, M.; Andreev, N.; Andriyash, I.; Artioli, M.; Aschikhin, A.; et al. EuPRAXIA conceptual design report. *Eur. Phys. J. Spec. Top.* **2020**, *229*, 3675–4284. [CrossRef]
26. PALLAS. Prototyping Accelerator Based on Laser-pLASma Technology—Project. 2023. Available online: http://pallas.ijclab.in2p3.fr (accessed on 23 February 2026).
27. LASERIX Laser Facility. 2023. Available online: http://laserix.ijclab.in2p3.fr (accessed on 23 February 2026).
28. Martelli, L.; Kononenko, O.; Andriyash, I.; Wheeler, J.; Gautier, J.; Goddet, J.P.; Tafzi, A.; Lahaye, R.; Giaccaglia, C.; Flacco, A.; et al. Physics of high-charge laser-plasma accelerators for few-MeV applications. *Phys. Rev. Appl.* **2025**, *23*, 034033. [CrossRef]
29. Oubrerie, K.; Leblanc, A.; Kononenko, O.; Lahaye, R.; Andriyash, I.A.; Gautier, J.; Goddet, J.P.; Martelli, L.; Tafzi, A.; Ta Phuoc, K.; et al. Controlled acceleration of GeV electron beams in an all-optical plasma waveguide. *Light Sci. Appl.* **2022**, *11*, 180. [CrossRef]
30. Ta Phuoc, K.; Corde, S.; Thaury, C.; Malka, V.; Tafzi, A.; Goddet, J.P.; Shah, R.; Sebban, S.; Rousse, A. All-optical Compton gamma-ray source. *Nat. Photonics* **2012**, *6*, 308–311. [CrossRef]
31. Yan, W.; Fruhling, C.; Golovin, G.; Haden, D.; Luo, J.; Zhang, P.; Zhao, B.; Zhang, J.; Liu, C.; Chen, M.; et al. High-order multiphoton Thomson scattering. *Nat. Photonics* **2017**, *11*, 514–520. [CrossRef]
32. Kozlova, M.; Andriyash, I.; Gautier, J.; Sebban, S.; Smartsev, S.; Jourdain, N.; Chaulagain, U.; Azamoum, Y.; Tafzi, A.; Goddet, J.P.; et al. Hard X rays from laser-wakefield accelerators in density tailored plasmas. *Phys. Rev. X* **2020**, *10*, 011061. [CrossRef]
33. Chaulagain, U.; Lamač, M.; Raclavský, M.; Khakurel, K.P.; Rao, K.H.; Ta-Phuoc, K.; Bulanov, S.V.; Nejdl, J. ELI Gammatron Beamline: A Dawn of Ultrafast Hard X-ray Science. *Photonics* **2022**, *9*, 853. [CrossRef]
34. Mo, M.; Chen, Z.; Fourmaux, S.; Saraf, A.; Kerr, S.; Otani, K.; Masoud, R.; Kieffer, J.C.; Tsui, Y.; Ng, A.; et al. Measurements of ionization states in warm dense aluminum with betatron radiation. *Phys. Rev. E* **2017**, *95*, 053208. [CrossRef]
35. Mahieu, B.; Jourdain, N.; Ta Phuoc, K.; Dorchies, F.; Goddet, J.P.; Lifschitz, A.; Renaudin, P.; Lecherbourg, L. Probing warm dense matter using femtosecond X-ray absorption spectroscopy with a laser-produced betatron source. *Nat. Commun.* **2018**, *9*, 3276. [CrossRef]
36. Giaccaglia, C.; Bayart, E.; Dubail, M.; Varma, C.; Heinrich, S.; Gautier, J.; Tafzi, A.; Kononenko, O.; Goddet, J.P.; Lamarre-Jouenne, I.; et al. Multiscale radiobiological assessment of laser-driven very high energy electrons versus conventional electrons. *bioRxiv* **2025**. [CrossRef]
37. Zhou, B.; Guo, Z.; Liu, S.; Wan, Y.; Liu, J.; Wang, H.; Pi, Y.; Guo, B.; Hua, J.; Lu, W. Dosimetric characterization of the laser-accelerated high-energy electron beam for radiotherapy applications. *Phys. Rev. Accel. Beams* **2025**, *28*, 111302. [CrossRef]
38. Mirzaie, M.; Li, S.; Zeng, M.; Hafz, N.; Chen, M.; Li, G.; Zhu, Q.; Liao, H.; Sokollik, T.; Liu, F.; et al. Demonstration of self-truncated ionization injection for GeV electron beams. *Sci. Rep.* **2015**, *5*, 14659. [CrossRef] [PubMed]
39. Espinos, D.O. High Quality Laser Driven Electron Beams for Undulator and Free Electron Laser Radiation. In *Accelerator Physics*; Université Paris-Saclay: Orsay, France; Ōsaka University, Faculty of Engineering: Osaka, Japan, 2021.
40. Kim, J.; Phung, V.; Roh, K.; Kim, M.; Kang, K.; Suk, H. Development of a density-tapered capillary gas cell for laser wakefield acceleration. *Rev. Sci. Instrum.* **2021**, *92*, 023511. [CrossRef] [PubMed]
41. Esarey, E.; Sprangle, P.; Krall, J.; Ting, A. Self-focusing and guiding of short laser pulses in ionizing gases and plasmas. *IEEE J. Quantum Electron.* **2002**, *33*, 1879–1914. [CrossRef]
42. Gori, F. Flattened gaussian beams. *Opt. Commun.* **1994**, *107*, 335–341. [CrossRef]
43. Couperus, J.P. *Optimal Beam Loading in a Nanocoulomb-Class Laser Wakefield Accelerator*; Technical Report; Helmholtz-Zentrum Dresden-Rossendorf: Dresden , Germany, 2018.
44. Derouillat, J.; Beck, A.; Pérez, F.; Vinci, T.; Chiaramello, M.; Grassi, A.; Flé, M.; Bouchard, G.; Plotnikov, I.; Aunai, N.; et al. Smilei: A collaborative, open-source, multi-purpose particle-in-cell code for plasma simulation. *Comput. Phys. Commun.* **2018**, *222*, 351–373. [CrossRef]
45. Massimo, F.; Beck, A.; Dérouillat, J.; Zemzemi, I.; Specka, A. Numerical modeling of laser tunneling ionization in particle-in-cell codes with a laser envelope model. *Phys. Rev. E* **2020**, *102*, 033204. [CrossRef]
46. Drobniak, P.; Baynard, E.; Bruni, C.; Cassou, K.; Guyot, C.; Kane, G.; Kazamias, S.; Kubytskyi, V.; Lericheux, N.; Lucas, B.; et al. Random scan optimization of a laser-plasma electron injector based on fast particle-in-cell simulations. *Phys. Rev. Accel. Beams* **2023**, *26*, 091302. [CrossRef]
47. Openfoam. Available online: https://www.openfoam.com/ (accessed on 23 February 2026).
48. Drobniak, P.; Baynard, E.; Beck, A.; Demailly, J.; Douillet, D.; Gonnin, A.; Iaquaniello, G.; Kane, G.; Kazamias, S.; Kubytskyi, V.; et al. Two-chamber gas target for laser-plasma electron source. *Rev. Sci. Instrum.* **2025**, *96*, 033304.
49. Openfoam. Available online: https://www.openfoam.com/documentation/guides/latest/doc/guide-applications-solvers-compressible-rhoPimpleFoam.html (accessed on 23 February 2026).

50. Openfoam. Available online: https://www.openfoam.com/documentation/guides/latest/man/interMixingFoam.html (accessed on 23 February 2026).
51. Available online: https://gitlab.in2p3.fr/cfd-simulations-lpa-target (accessed on 23 February 2026).
52. Steinke, S.; Van Tilborg, J.; Benedetti, C.; Geddes, C.; Schroeder, C.; Daniels, J.; Swanson, K.; Gonsalves, A.; Nakamura, K.; Matlis, N.; et al. Multistage coupling of independent laser-plasma accelerators. *Nature* **2016**, *530*, 190–193. [CrossRef] [PubMed]
53. Samarin, G.; Zepf, M.; Sarri, G. Radiation reaction studies in an all-optical set-up: Experimental limitations. *J. Mod. Opt.* **2018**, *65*, 1362–1369. [CrossRef]
54. Monzac, J.; Smartsev, S.; Huijts, J.; Rovige, L.; Andriyash, I.A.; Vernier, A.; Tomkus, V.; Girdauskas, V.; Raciukaitis, G.; Mackevičiūtė, M.; et al. Optical ionization effects in kHz laser wakefield acceleration with few-cycle pulses. *Phys. Rev. Res.* **2024**, *6*, 043099.
55. Monzac, J.; Smartsev, S.; Huijts, J.; Rovige, L.; Andriyash, I.A.; Vernier, A.; Tomkus, V.; Girdauskas, V.; Raciukaitis, G.; Mackevičiūtė, M.; et al. Differential pumping for kHz operation of a laser wakefield accelerator based on a continuously flowing hydrogen gas jet. *Rev. Sci. Instrum.* **2025**, *96*, 043302. [CrossRef] [PubMed]
56. Thévenet, M.; Mittelberger, D.E.; Nakamura, K.; Lehe, R.; Schroeder, C.B.; Vay, J.L.; Esarey, E.; Leemans, W.P. Pulse front tilt steering in laser plasma accelerators. *Phys. Rev. Accel. Beams* **2019**, *22*, 071301. [CrossRef]
57. Löfquist, E.; Gustafsson, C.; Angella, A.; Persson, A.; Lundh, O. Correlated X-ray and electron beam steering by pulse-front tilt in laser wakefield acceleration. *Phys. Rev. Accel. Beams* **2025**, *28*, 102802. [CrossRef]
58. Pak, A.; Marsh, K.; Martins, S.; Lu, W.; Mori, W.; Joshi, C. Injection and trapping of tunnel-ionized electrons into laser-produced wakes. *Phys. Rev. Lett.* **2010**, *104*, 025003. [CrossRef]

Disclaimer/Publisher's Note: The statements, opinions and data contained in all publications are solely those of the individual author(s) and contributor(s) and not of MDPI and/or the editor(s). MDPI and/or the editor(s) disclaim responsibility for any injury to people or property resulting from any ideas, methods, instructions or products referred to in the content.